Ultra rapid direct heating synthesis of ZnO nanorods with improved light trapping from stacked photoanodes for high efficiency photocatalytic water splitting

Article (Accepted Version)

Ultra Rapid Direct Heating Synthesis of ZnO Nanorods with Improved Light Trapping from Stacked Photoanodes for High Efficiency Photocatalytic Water Splitting

Ultra Rapid Direct Heating Synthesis of ZnO Nanorods with Improved Light Trapping from Stacked Photoanodes for High Efficiency Photocatalytic Water Splitting

Wei Cheat Lee[a], Yuanxing Fang[a], Daniel Commandeur[a], Rong Qian[b*], Zainab T. Y. Al-Abdullah[a] and Qiao Chen[a*]

[a]Chemistry Department, School of Life Sciences, University of Sussex, Brighton, BN1 9QJ, UK

[b]National Center for Inorganic Mass Spectrometry in Shanghai, Shanghai Institute of Ceramics, Chinese Academy of Science, Shanghai 200050, P. R. China

[*]Corresponding authors.

E-mail addresses:

qianrong@mail.sic.ac.cn (Rong Qian)
qiao.chen@sussex.ac.uk (Qiao Chen)

Abstract

An ultra rapid growth method for vertically aligned ZnO nanorod (NR) thin films on metal meshes is developed using a direct heating synthesis (DHS) technique. A typical nanorod growth rate of 10 μm/hr was achieved. The effects of the applied heating powers and growth durations on the morphologies of ZnO nanostructures were examined. High density surface defects were formed on the ZnO NRs, which is responsible for slow charge recombination and high efficiency in the photoelectrochemical (PEC) water splitting process. The light absorption for a photoanode was significantly improved by light trapping using a 3D stacked metal mesh photoanode structure. With the internal reflection between the stacked photoanodes, the final light leakage is minimised. The light absorption in the stacked photoanode is improved without restricting the charge transportation. In comparison with a single mesh photoanode and a chemical bath deposition (CBD) grown flat photoanode, the PEC water splitting efficiency from the stacked photoanode was increased by a factor of 2.6 and 6.1 respectively.

Keywords: Photoelectrochemical water splitting, Direct heating synthesis, Zinc oxide nanorods, Light trapping, Mesh substrate, Stacked photoanode.

1. Introduction

The development of renewable energy sources has steadily grown to replace the conventional fossil fuel energy source. Photoelectrochemical (PEC) water splitting is one of the promising solutions to harvest and store the solar energy into hydrogen fuels. Photocatalysts with low recombination losses and good electrical contact to the substrates are essential for a high efficient photoconversion [1]. Nanostructured metal oxides, such as TiO_2 and ZnO, have been demonstrated with potential application in PEC water splitting. In particular, ZnO has received great attention due to its wide direct band gap, large exciton binding energy and high quantum efficiency [2]. ZnO has a longer hole diffusion length (~125 nm) [3] in comparison to TiO_2 (~100 nm) [4] and its electron mobility is typically 10-100 times higher than that of TiO_2 [5, 6]. One of the most interesting ZnO nanostructures as a photoanode is the vertically aligned nanorods (NRs), which offers a large surface area and excellent electrolyte transportation [7]. So far, vertically aligned ZnO NR arrays can be synthesised through CBD, hydrothermal growth and chemical vapour deposition methods [8-10]. However, such growth processes are generally slow with a typical deposition rate of 0.5 μm/hr in the NR length.

Here, we report for the first time an ultra rapid method for the synthesis of vertically aligned crystalline ZnO NR arrays on stainless steel (SS) meshes. The substrate is heated directly by applying an electrical current through, namely direct heating synthesis (DHS). The formation of ZnO was localised on the hot surface of the mesh wires. A high density of defects and charge carriers were formed in the ultra rapid DHS process, which is responsible for the significantly increased PEC efficiency.

Although the NR structure offers large surface area allowing sufficient contact between the electrolyte and photocatalyst surface reaction centres, it could suffer from poor charge transport through the photocatalyst if the NRs are too long. Very often, the film thickness is

reduced for optimised charge transportation, which decreases the light absorption [11, 12]. As such, additional technology has been used to enhance light trapping and light absorption [13]. Light absorption can be extended and improved by sensitising with dyes and quantum dots [14], while light trapping can be achieved by applying an anti-reflection coating; nano textures were developed, although they are normally complicated and expensive [15]. Recent research has also identified that increasing the density of oxygen vacancy could improve charge separation and thus photocatalytic efficiency [16].

Metal mesh substrates have been used to increase the effective surface area. TiO_2 nanoparticles deposited on SS mesh have been shown to enhance the efficiency of dye-sensitised solar cells [14]. A great number of 1D metal oxide nanostructures, such as nanorods (NRs) [17], nanotubes [18], nanosheets [19] and nanowires [20] have been also been prepared on wires [18, 21] and meshes [22, 23] for improving photoconversion efficiency.

Here, we present a simple but effective method of trapping light by using stacked multiple photoanodes based on metal mesh substrates. The SS mesh allows a percentage of light to be transmitted through. This transmitted light will be trapped by reflection between layered photoanodes in a stacked mesh photoanode structure, which minimises light leakage. In comparison with a single layer SS mesh photoanode, the 4-layer stacked mesh photoanode gave a factor of 2.5 enhancement in the photoconversion efficiency.

2. Experimental

2.1 Direct heating synthesis (DHS) of ZnO nanorods on SS mesh

All the chemicals used were analytical grade and purchased from Sigma-Aldrich. SS woven meshes with square opening (hole size 0.142 mm and wire diameter 0.112 mm) were used as substrates. The mesh was cut into a rectangular shape (1 cm x 3 cm) and spot welded onto two SS bars. The experimental setup is shown in Fig. S1 in the Supporting Information.

The samples were degreased and cleaned under sonication in an isopropanol (IPA) bath and deionised (DI) water for 15 minutes each. They were then dried in air before used as substrates for growing ZnO NRs with the DHS method. A bench top DC power supply with maximum output current of 60 A was used for direct heating by passing the DC current directly through the SS mesh immersed in the growth solution. The applied power was regulated and controlled from 14 to 60 W at different heating durations varying from 30 to 120 min.

The nutrient solution was composed of a 1:1 molar ratio of zinc nitrate hexahydrate (0.89 g) and hexamethylenetetramine (HMT; 0.42 g) dissolved in 150 ml DI water. The final concentration of Zn^{2+} in the growth solution was 20.0 mM. The mounted SS mesh was then immersed in the nutrient solution for growing ZnO NRs. One thermocouple was spot-welded onto the SS mesh to measure the substrate temperature, while another thermocouple was immersed in the growth solution to monitor the solution temperature. In addition, a thermal imaging camera, FLIR One, was used to map the temperature distribution during the DHS. The samples were then allowed to cool to room temperature, rinsed three times with DI water and air dried.

In order to improve light trapping and absorption, multiple layers of mesh photoanodes were stacked in parallel with a fixed separation of 5 mm.

2.2 Characterisation

The surface morphologies were studied by scanning electron microscopy (SEM, JSM 820M, Jeol). The crystallinity, crystal orientation and crystal alignment of the nanostructures were analysed by powder x-ray diffraction (XRD, Siemens D500). The average diameter and average film thickness were measured from top- and cross-sectional SEM images using Image J software (National Institute of Health, USA). The optical transmission spectra were recorded using a UV-visible spectrophotometer (Thermospectronic UV 300). The PEC water

splitting was measured in 1.0 M KOH electrolyte (pH 13.6) using a standard three-electrode configuration. A platinum foil was used as counter electrode and a saturated Ag/AgCl electrode was used as a reference electrode. A USB potentiostat (eDAQ) was used to control and record the photocurrent as a function of electrochemical potential. Sunlight was simulated using a 300 W xenon arc lamp with an AM1.5 G filter and the output light power density was adjusted to 100 mW cm^{-2}. The optical power density was calibrated by a power meter (Newport 1830-C) with a wide band sensor (Newport 818-UV attenuated). Charge carrier densities were measured using electrochemical impedance measurements (EIS, Palmsens 3.0) in 0.5 M Na_2SO_4 solution (pH 6.8) with 10 mV of the AC signal.

3. Results and Discussion

3.1 The growth of ZnO NRs on SS meshes by DHS method

A typical CBD growth of ZnO NR involves the decomposition of HMT above 85°C to increase the pH of the nutrient solution. At higher pH, Zn^{2+} is hydrolysed into $Zn(OH)_2$, which converts to ZnO onto the substrate. In our DHS synthesis process, the conductive substrate sample is heated by passing a current directly. A thermal image was recorded at the beginning of the DHS process, shown in Fig. 1A. It is clear that the SS substrate and its surrounding were heated up rapidly. The temperature of the SS mesh and nutrient solution were also monitored with thermocouples as a function of applied power, shown in Fig. 1B. When the applied power was increased, the temperatures of both the SS mesh and the nutrient solution were increased. However, the SS mesh is much hotter than the nutrient solution at a high heating power since the solution is heated by the thermal dissipation from the hot SS wires in the mesh. The temperature of the SS mesh at 33 W is ~83°C, which is similar to the CBD growth temperature, ~85°C.

The unique DHS heating process guarantees that the growth process is initiated on the surface of the substrate, which has several advantages. First, unlike the conventional CBD or hydrothermal growth, the DHS is a one-step process where the seeds naturally occurred during the initial growth process on the hot surface. Second, the fast direct heating of the substrate facilitates an ultra-rapid growth process. For instance, to grow ZnO NRs with a length of ~5 µm, a typical CBD or a hydrothermal method requires more than 10 hours [7, 24], giving a growth rate of ~0.5 µm/hr. With DHS, the growth time is reduced to 30 minutes at 33 W heating power, which gives a nominal growth rate of 10 µm/hr. This represents an increase of growth rate by a factor of 20. Third, DHS is an in-situ heating process where the heat is uniformly generated on the substrate even for large size sample, which is essential for homogenous deposition of ZnO NRs. The concentrated heat on the SS mesh wires will rapidly decompose the HMT and encourage the deposition of ZnO only on the hot surface, resulting in minimum chemical waste and ultra-rapid growth of homogenous NR films.

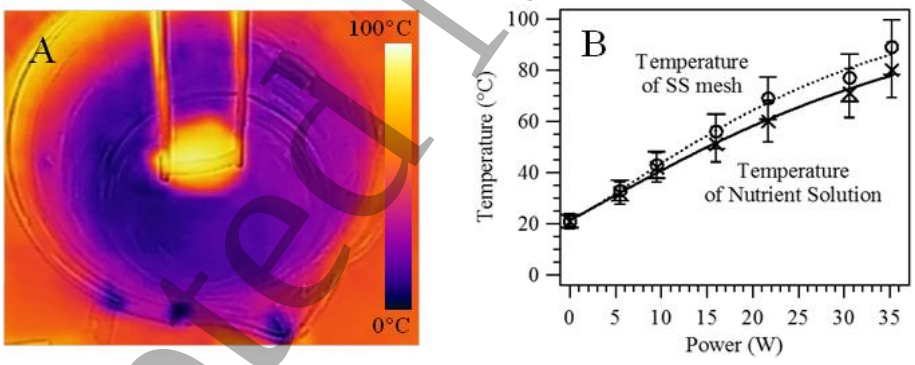

Fig. 1. (A) Thermal image of DHS heated sample in the growth solution. (B) Temperature of SS mesh (1 x 3 cm^2) and nutrient solution (150 ml) as a function of applied heating power after being heated for 10 min.

Fig. 2A and B represent the photographs of SS meshes before and after the growth of ZnO NRs in 150 ml of nutrient solution for 60 minutes at an applied heating power of 33 W. It is clear that after the deposition of ZnO NRs, the optical transparency is significantly

reduced although the sample is still translucent. Also, the colour of the SS mesh was changed from shiny-grey to white-grey.

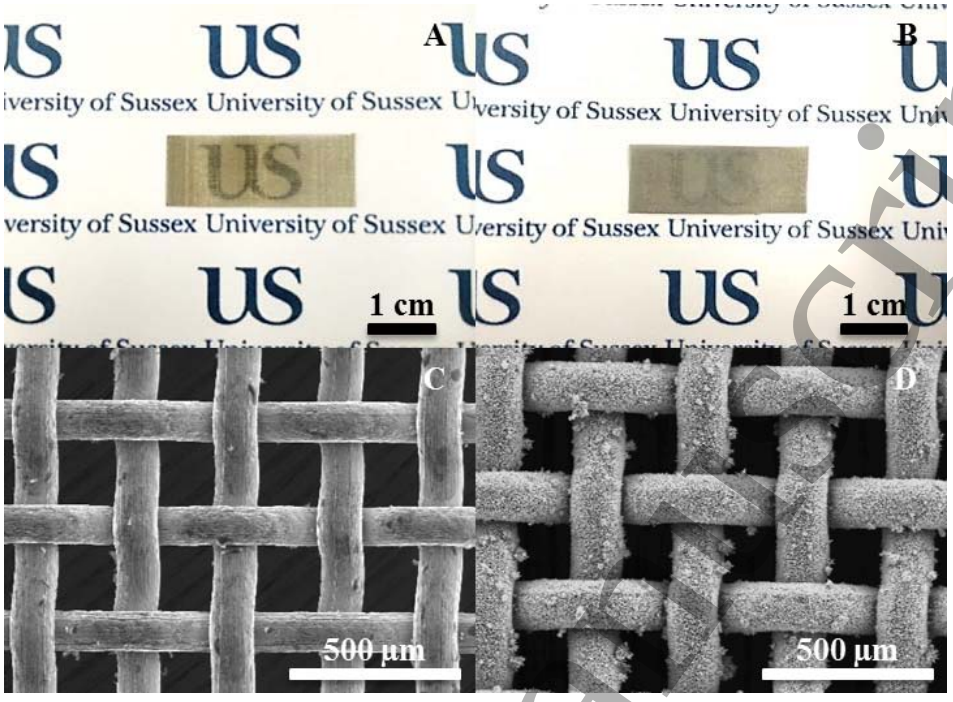

Fig. 2. Photographs of SS meshes (A) before and (B) after DHS growth of ZnO NRs for 60 minutes. (C) and (D) are the corresponding top view SEM images.

The low magnification SEM images of SS mesh before and after the growth of ZnO NRs are shown in Fig. 2C and 2D. The original SS mesh has an open square of 0.142 mm with a wire diameter of 0.112 mm. After 60 minutes of DHS reaction, ZnO NRs were uniformly deposited in a radially outward direction on the surface of SS wires throughout the SS mesh without any obvious cracks. The length of the NRs was measured to be 9.6 µm. Using Equation 1 specified in Fig. S1 in the Supporting Information, the opening area of the clean SS mesh and the DHS sample are ~31.25% and ~23.37%, respectively.

3.2 Effect of applied power on the morphology of ZnO NRs

Temperature determines the growth kinetics and thus the nanomorphology of ZnO NRs. In a DHS process, the growth temperature is determined by the applied heating power, shown in Fig. 1B, which is used to control the morphology of ZnO NRs. All the other

experimental conditions, including the dimension of SS mesh (1 × 3 cm^2), growth duration (60 minutes) and volume and concentration of the nutrient solutions (150 ml, 20 mM) were maintained as constant. The applied heating powers were operated ranging from 14.0W to 60.0W.

Fig. 3 demonstrates that the final morphology of ZnO NRs is strongly affected by the applied heating power. At low applied power, 14.0 W, only some sparse randomly oriented ZnO NRs with some large crystals were formed, Fig. 3A. By increasing the applied power to 33 W, high density, well-ordered and vertically aligned ZnO NRs were uniformly formed, Fig. 3C. Further increasing the power to 45.5 W, tapered ZnO NRs with a sharp tip and larger diameter were formed, Fig. 3D. Some small branches could also be observed. At 60.0 W, the branched and tapered ZnO NRs were formed, Fig. 3E.

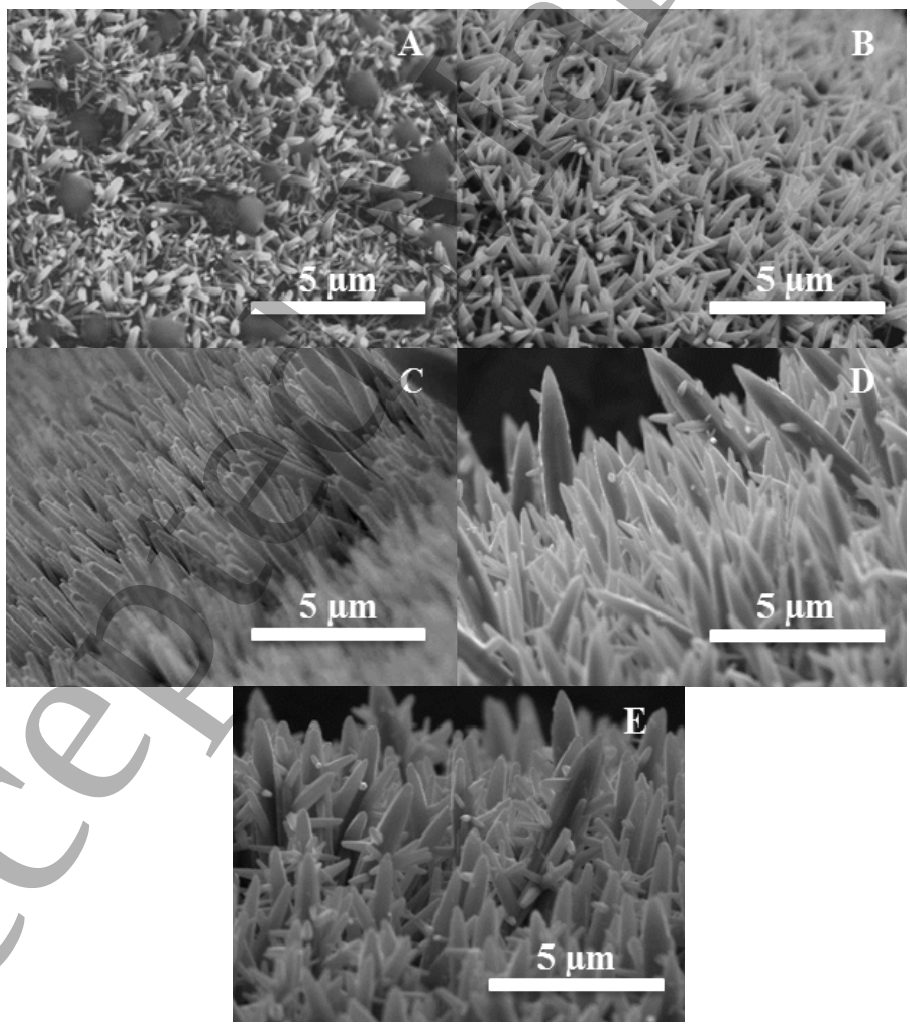

Fig. 3. SEM images of ZnO NRs grown on SS meshes for 60 minutes at the heating power of (A) 14.0W, (B) 22.5W, (C) 33.0W, (D) 45.5W and (E) 60.0W.

The morphology of the NRs is determined by the balance between the HMT decomposition rate and the ZnO formation rate. During the DHS, ZnO small crystals will be formed in the first few minutes, which serve as the seeds for the growth of vertically aligned ZnO NRs. At low heating power, the temperature of the substrate increases slowly, resulting in the slowly decomposition of HMT. This allows a significant Ostwald ripening to form large crystals as observed in Fig. 3A. At 33 W, the temperature of the SS mesh is ~83°C, the HMT decomposition rate (~85°C) and the ZnO growth rate are balanced, resulting in formation of good quality ZnO NRs.

By applying high heating power (above 33 W), the decomposition of HMT is much faster than the formation of ZnO, which promoted the secondary nucleation. Thus, branched NRs were observed. It is also noted that the tapered ZnO NRs were formed at high power and high growth temperature, as shown in Fig. 3D and E. This is due to localised heating on the base of the nanorods, which create high temperature gradient along the c-axis of NRs. The base of the NRs is hotter than the tip and therefore has high growth rate. The observed heating power dependence of the NR morphology is illustrated in a schematic diagram in Fig. S2 (Supporting Information). As the heating power of 33 W gives the optimal morphology of the ZnO NRs, this power was used in the following studies.

3.3 Effect of growth duration on the morphology of ZnO rods

While maintaining other growth parameters, the effect of growth duration on the morphology of ZnO NRs was also investigated, shown in Fig. 4. It is clear that increasing the growth duration will lead to an increase the length and the diameter of ZnO NRs.

As shown in top view SEM images in Fig. 4A-D, the ZnO NRs were homogenously deposited without any cracks. Smooth interfaces were seen between ZnO NRs and the surface

of the SS wires, shown in cross-sectional SEM images, implying the good adhesion of ZnO NR films. Increasing the duration of reaction results in longer and wider ZnO NRs.

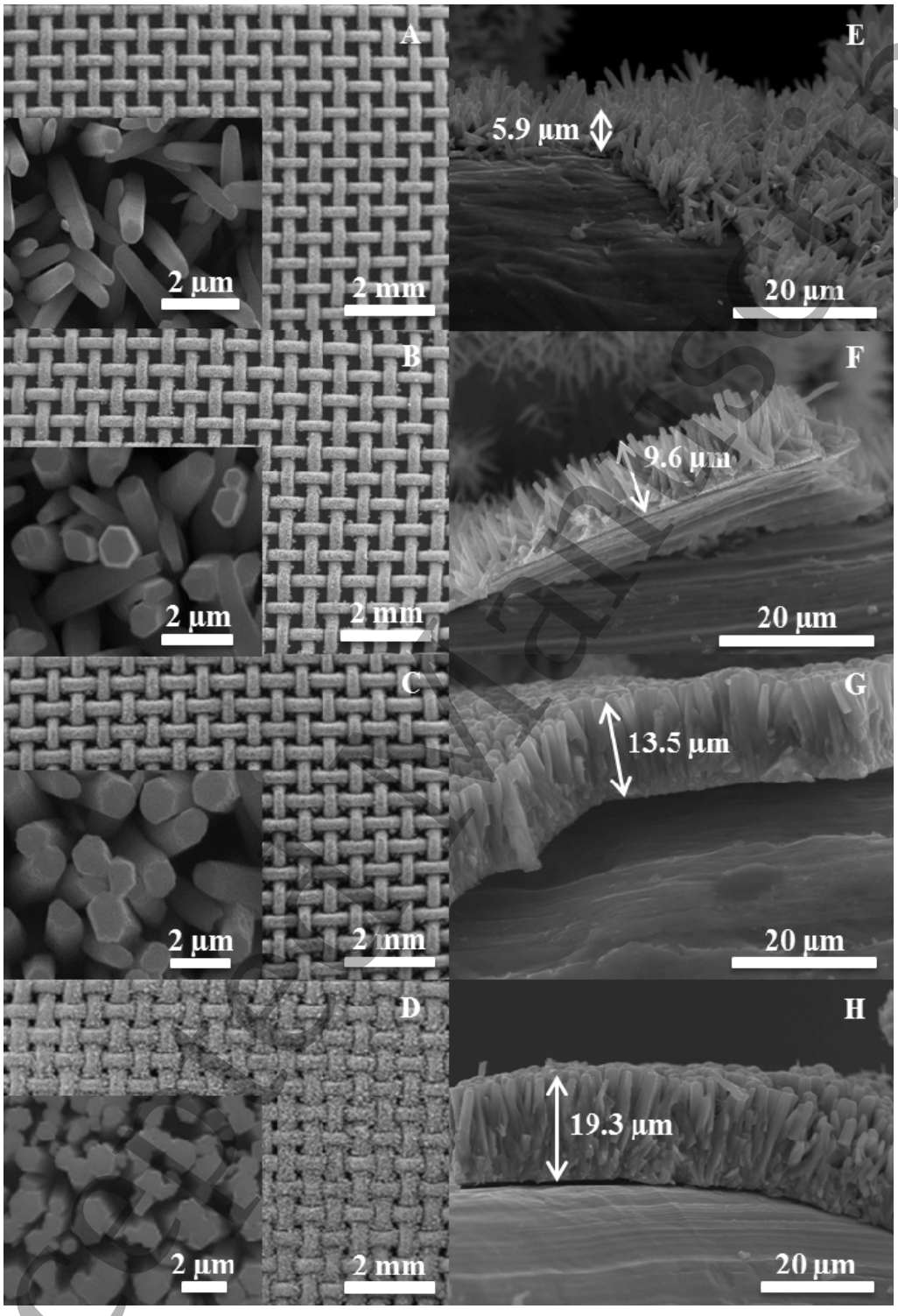

Fig. 4. Top and cross-sectional view SEM images of ZnO NRs on SS meshes at an applied heating power of 33 W in 150 ml of nutrient solution for 30 (A, E), 60 (B, F), 90 (C, G) and 120 min (D, H). The insets show the high resolution SEM images. The samples were scratched to reveal the cross-section view in the side-view images (E-H).

The measured length and diameter of the ZnO NRs are plotted in Fig. S3C (Supporting Information). Between 30 and 120 min of growth, the average diameter of NRs increased linearly from 483±95 to 1280±105 nm and the length of ZnO rods also increased linearly from 5.9 μm to 19.3 μm. Meanwhile, the percentage of open area of the SS meshes is reduced from 26.28%, to 15.94%, Fig. S3B (Supporting Information). It is worth noting that after 120 minutes growth, only small opening gaps are left in the mesh, as shown in Fig. 4G. This will significantly affect the optical properties of the SS mesh. The optical transmission was measured, as shown in Fig. S3A and S3B, Supporting Information. It reveals that the optical transmission is linearly decreased from 30.74% to 15.05% as the growth duration is increased. For comparison, both the optical transmittance and the opening area percentages were plotted as a function of growth duration in Fig. S3B (Supporting Information).

The crystal structure and crystal orientation of the as-grown samples were investigated by powder XRD (Fig. S4A, Supporting Information). All the XRD peaks were assigned to wurtzite structure of ZnO with no appearance of other additional peaks. Both the texture coefficient [25] and the crystal domain [26] of ZnO NRs grown at different durations were calculated (Fig. S4B, Supporting Information). The results demonstrate that both the texture coefficient and crystal domain of the samples are increased when the growth duration is increased, suggesting that both the crystal orientation and crystal quality were improved.

3.4 PEC hydrogen generation

3.4.1 Photocatalytic activity of ZnO NRs on SS plate and SS mesh

The water photoelectrolysis activity ZnO NRs on SS mesh photoanode was evaluated by measuring the photocurrent in 1.0 M KOH aquatic electrolyte under the illumination of an AM1.5 G solar simulator. We choose the DHS sample grown for 30 min at 33 W heating power as the testing photoanode, because it gives good quality NRs with typical length of 5.9

μm. The vertically aligned ZnO NRs on an SS plate was obtained after 15 hours of CBD growth, which gives a similar length of 5.3 μm, shown in Fig. S5A in supporting information. For comparison, the ZnO NRs on a SS mesh sample was also synthesised using standard CBD method with a growth duration of 15 hours. The DHS mesh sample is referred to as M30, the plate sample is referred to as P15 and the CBD mesh sample is referred as CBD-M15H. Here, the numbers signify the growth duration.

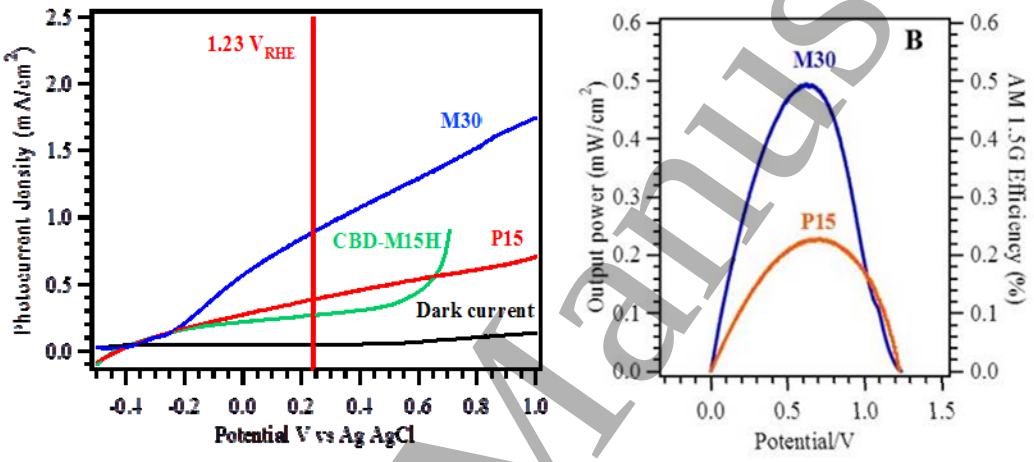

Fig. 5. (A) Photocurrent generated from M30, P15 and CBD-M15H together with the dark current measured from M30 and (B) corresponding PEC output power and photoconversion efficiency under AM1.5 G solar irradiation.

Fig. 5A shows the current-voltage (*I-V*) curves for M30, P15 and CBD-M15H photoanodes in the dark and under simulated sunlight in the potential range from –0.5 to 1.0 V referenced to the KCl saturated Ag/AgCl potential (0.1976 V at 25ºC). For an electrolyte of 1.0 M KOH with pH 13.6, the reversible oxygen standard potential is at 0.23 $V_{Ag/AgCl}$, marked with the red line in Fig. 5A. With light on, the photocurrent densities from P15 and CBD-M15H increase almost linearly with onset potential (open circuit potential) of –0.40 $V_{Ag/AgCl}$. Although similar onset potential was achieved, the M30 photoanode gives much higher photocurrent. For measurements at 1.23 V_{RHE}, it generated 0.88 mA/cm^2 in comparison to 0.38 and 0.25 mA/cm^2 from P15 and CBD-M15H photoanodes. For both M30 and P15

samples, photocurrent generated does not reach a plateau. This indicates the charge recombination and interface reaction kinetics did not limit the generation of photocurrent under our experimental conditions. The photocurrent density from CBD-M15H is much lower than that from M30. With the potential higher than 0.65 VAg/AgCl, the current increases rapidly. This is due to the electrolysis of water by the exposed bare metal of the SS mesh. Similar increases was found for the dark current. The photoconversion efficiencies from M30 and P15 samples were calculated based on the ratio of electrochemical energy density to the input of photo energy density [27], shown in Fig. 5B. A much higher output power density, and thus higher photoconversion efficiency, was found for the M30 photoanode, with a maximum output power of 0.49 mW/cm^2 (0.49%), relative to the 0.23 mW/cm^2 (0.23%) from the P15 photoanode.

In order to understand the intrinsic electronic properties of the M30 and P15 in electrolyte, the capacitance between the ZnO NR semiconductor and electrolyte was evaluated using EIS measurements. Both charge carrier densities and flatband potentials were obtained by the Mott-Schottky (M-S) analysis [28]. Fig. 6 shows the M-S plots from P15 and M30. The capacitance values were measured in 0.5 M of Na_2SO_4 in the dark at 1 kHz 10 mV modulation. P15 and M30 photoanodes gave similar results, with value of −0.38 $V_{Ag/AgCl}$ in agreement with the literature [29]. This is normally determined by the chemical elements and their crystal structures, therefore it is not surprising that P15 and M30 photoanodes have the same values.

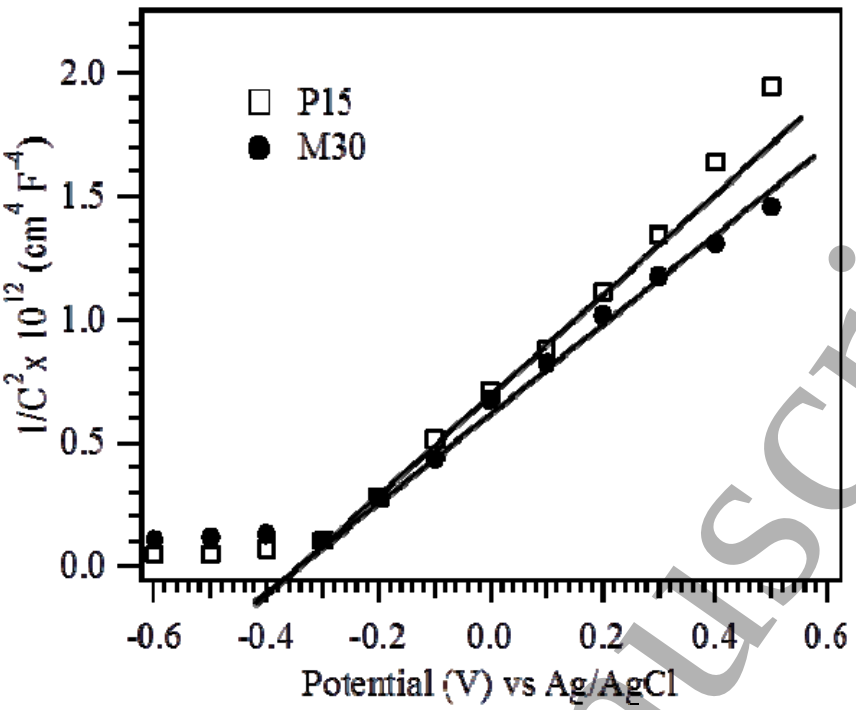

Fig. 6. Mott-Schottky plots of P15 and M30 measured in 0.5 M Na_2SO_4 solution in the dark with a frequency of 1 kHz. The amplitude of the sinusoidal wave was set at 10 mV.

The positive slopes of the M-S plots confirm ZnO is an n-type semiconductor where the majority of charge carriers are electrons. The slopes of the M-S plots were used to derive the charge carrier densities [30, 31]. The calculated electron densities were 6.15×10^{18} cm^{-3} and 8.22×10^{18} cm^{-3} for P15 and M30 photoanodes, which are comparable to the typical value of 6×10^{18} cm^{-3} for the ZnO NRs [32]. However, the DHS-grown ZnO NRs on the SS mesh (M30) have a charge carrier density about 33% greater than that of P15.

With increased defect density, such as oxygen vacancy, the average Zn-O bond length in the ZnO crystal, *L*, will also be reduced. By calculating the lattice parameters, *a* and *c*, from the diffraction angles, one can calculate the *L* value [33]. For P15 and M30 photoanodes, Zn-O bond lengths of 1.97 and 1.92 Å were identified. These values are smaller than the reported value of 2.21 Å [33]. This observation also confirms that M30 has higher density of structural defects than P15, which are normally associated with higher density of oxygen vacancies.

The presence of a high density of defects within the ZnO NRs is also evident from the XRD peak width. The (002) diffraction peak from M30 is much broader than that of P15, shown in Fig. S5B in the supporting information. This observation is consistent with the high defect density in M30 ZnO NRs. The high carrier density and defect density can be attributed to the ultra-rapid growth of ZnO NRs in the DHS process. Such increases could not only enhance the charge transport in ZnO but also improve the electron transfer at the interface between the ZnO and SS substrate [34].

The effects of carrier density and charge mobility on PEC performance can also be observed from photocurrent transient dynamics, signified by the onset of photocurrent spikes when the light is switched on. The observed photocurrent is determined by the rate of excited electron-hole pair generation, the rate of holes moving towards the surface of the photoanode, and the rate of water oxidation. When the surface reaction (water oxidation) becomes the rate-limiting process, the photocurrent will show an initial spike with light onset, which will gradually decrease to a stable value. The excess excited electron-hole pairs will be recombined, resulting in a reduced photoconversion efficiency [22, 35]. Fig. 7A and B illustrates the transient photocurrent measurements from P15 and M30 samples as a function of light irradiation intensity. The samples were biased at 1.00 V_{RHE}.

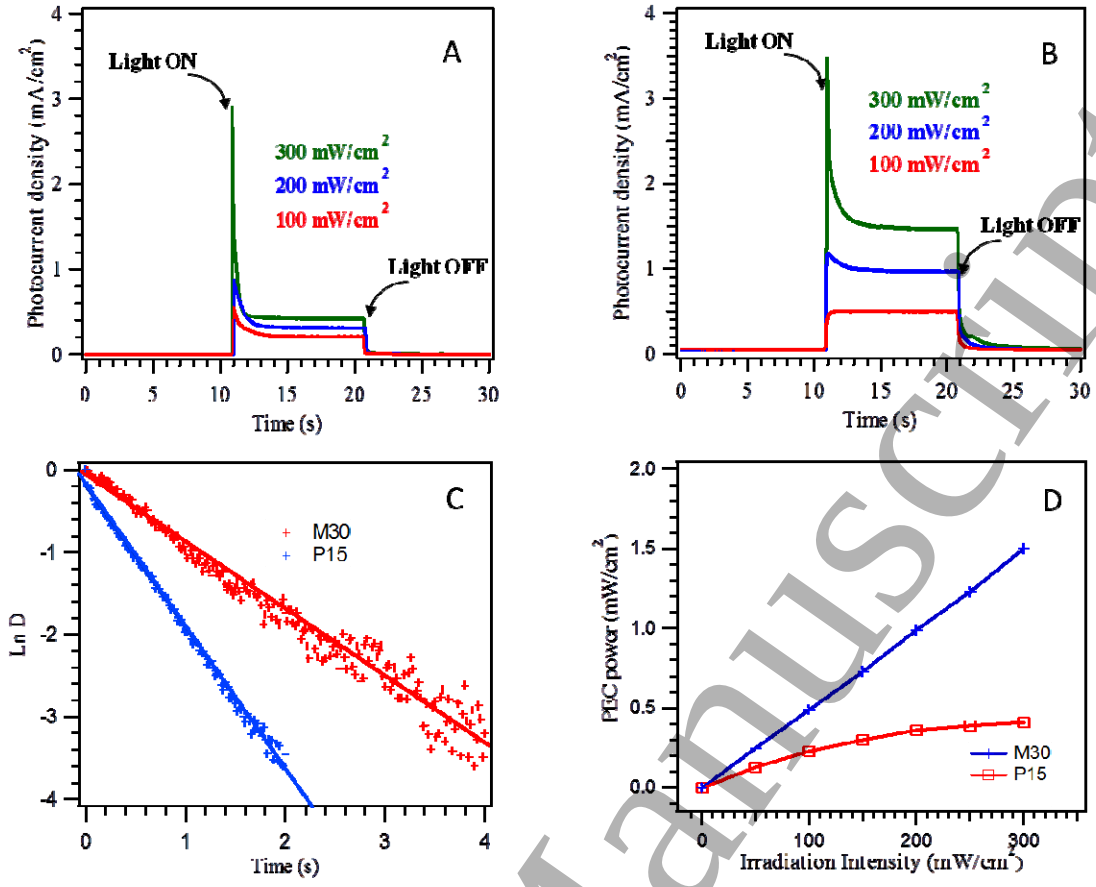

Fig. 7. Transient photocurrent (at 1.00 V_{RHE}) obtained with light on and off under different irradiation intensities for (A) P15 and (B) M30. (C) The exponential decay of normalised photocurrent *D* measured at 1.00 V_{RHE} under 200 mW/cm^2 irradiation. (D) PEC output power as a function of radiation intensity from P15 and M30.

It is clear that for the P15 sample, a photocurrent spike (I_{in}) was observed initially under an illumination power as low as 100 mW/cm^2 and its intensity increases with light intensity, shown in Fig. 7A. These spikes are a result of the slow oxygen evolution reaction kinetics and/or low charge mobility of the semiconductor [36, 37]. The photocurrents decay immediately after the sudden illumination until a stationary photocurrent (I_{st}) is attained. The concentration of excitons and the charge recombination rate are increased when the illumination intensity increases, which was observed from both P15 and M30 samples. Although similar spike intensities were observed from both samples, the steady photocurrents (I_{st}) achieved from M30 are much higher than those from P15. This suggests that the M30 sample has a higher surface reaction rate, which is directly related to the higher density of

surface defect centres. The generation of defects in metal oxide semiconductor is directly linked to the growth temperature. The high surface density of defects in M30 can be attributed to the direct heating mechanism. During the DHS process, the hottest point is always on the metal mesh wire. For an individual ZnO NR, its core is attached to the heated metal wire and its surface is in contact with growth solution. Thus the core of ZnO NR is hotter than the surface, which will naturally result in high surface density. In contrast, the CBD growth is a slow process with homogeneous temperature. Therefore, the ZnO NRs from CBD will have less density of defects, which is consistent with the charge carrier density measurements.

The exponential decay in the transient photocurrent, I_t, suggests the charge recombination follows first order kinetics, determined by the concentration of minority charge carriers. Within a small time interval, Δt, this concentration can be calculated as $(I_t\text{-}I_{st})\Delta t$, calibrated with respect to I_{st}. For a fixed time interval, this concentration is proportional to $(I_t\text{-}I_{st})$, which can be normalised to a unitless parameter, D, as $(I_t\text{-}I_{st})/(I_{in}\text{-}I_{st})$ [35]. With first order kinetics, the charge recombination rate can be calculated from the slope of the ln D vs t curve. Fig. 7C shows such kinetic plots at the applied potential of 1.00 V_{RHE} under 200 mW/cm^2 irradiation. The measured charge recombination rate constants are 1.81 and 0.84 s^{-1} for P15 and M30 samples, which give the half-life of 0.38 and 0.82 s respectively. The lower recombination rate constant and longer charge survival time from the M30 sample is directly related to the higher I_{st} and photoconversion efficiency. Similar values of recombination time were obtained from ZnO NRs measured by intensity modulated photovoltage spectroscopy [38].

The PEC output power was also measured as a function of irradiation power up to 300 mW/cm^2, shown in Fig. 7D. It is clear that for the P15 sample the photocurrent suffers from power saturation, while for the M30 sample the photocurrent increases linearly up to the

maximum applied photoenergy density. This is related to the higher charge carrier density and higher photoconversion efficiency from the M30 photoanode. The surface reaction and charge transportation are not the limiting factors for the photoconversion. Fig. S6 in the Supporting Information shows the anodic photocurrent dynamics from P15 and M30 photoanodes under repeated light on-off cycles for 150 s at different irradiation intensities of 100, 200 and 300 mW/cm^2. The transient dynamic behaviour is stable and there is obvious degradation in PEC performance. However, the photocurrent output decrease was observed after 1 hr of the PEC reaction, which is due to the slow dissolution of ZnO nanorods in the alkaline solution.

In addition, larger effective surface area of metal mesh photoanode could be responsible for the higher photocatalytic activity of M30 photoanode. This larger surface area is related to the corrugated 3D morphology of the mesh with respect to the flat substrate. The detailed calculation for the effective surface area of the SS mesh is shown in Fig. S7 in the Supporting Information. The total effective surface area of the SS mesh was found to be 1.23 cm^2, which is higher than a flat substrate of 1 cm^2. This will support more ZnO NRs and offers a larger number of reaction sites with improved light absorption efficiency.

3.4.2 Effect of the ZnO NR thickness on photocatalytic activity

The PEC performance of ZnO NRs on SS meshes at different growth durations were also examined. Fig. 8A demonstrates the *I-V* curves from sample grown in 30 (M30), 60 (M60), 90 (M90) and 120 min (M120) together with the dark current from M120 in the potential range of –0.5 to 1.0 $V_{Ag/AgCl}$. As shown in Fig. S3C in the Supporting Information, the length of the ZnO NRs increases linearly as a function of growth duration. Fig. 8A shows that increasing growth duration does not have any obvious effect on the open-circuit photopotentials. However, the photocurrent density does increase as the ZnO NRs become

longer. At a typical potential of 1.23 V_{RHE}, the photocurrent generated from M30, M60, M90 and M120 were measured to be 0.78, 0.92, 0.98 and 1.05 mA/cm^2, respectively.

Fig. 8B presents the corresponding output power and photoconversion efficiencies. Consistent with the photocurrent, the highest photoconversion output power and efficiency were achieved from the thickest ZnO NR photoelectrode (M120). This is because the longer ZnO NRs absorb more light with larger effective surface area [9, 39].

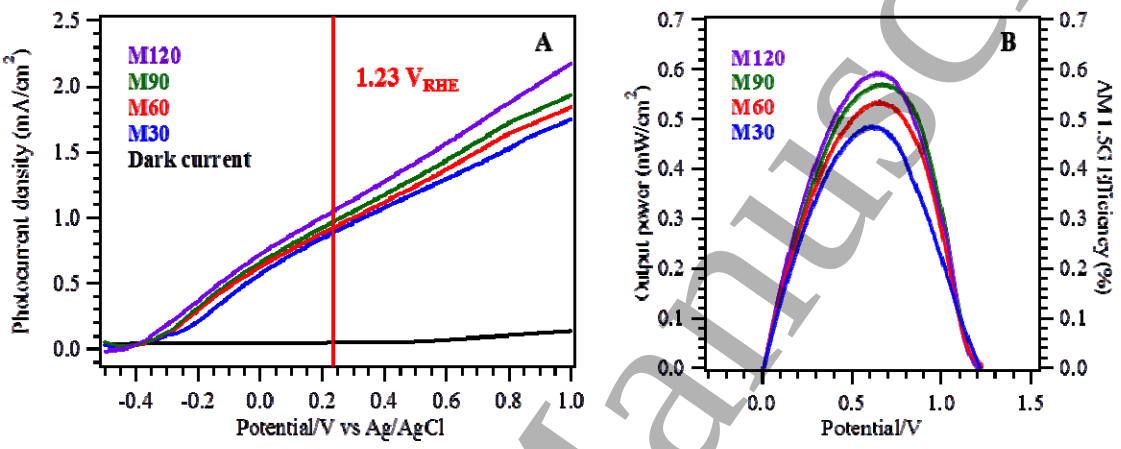

Fig. 8. (A) *I-V* curves of ZnO NRs at different growth durations together with dark current measured from M120 and (B) corresponding PEC output power and photoconversion efficiency under AM1.5 G full solar spectrum irradiation.

Although increasing the growth duration did lead to a higher photoconversion efficiency, such improvement is much slower than the increase of the ZnO NR length. For example, although the film thickness of M120 is ~325% thicker than that of M30, the conversion efficiency only shows an enhancement of ~23%.

This can be attributed to several possible mechanisms. First, by increasing the length, the electrical potential gradients along the longer axis of NRs is reduced [22]. This will decrease the mobility of the excited electrons, which also need to travel longer distance for longer ZnO NRs, increasing the exciton recombination probability. This decreases the benefit of improved light absorption and limits the increase of photoconversion. Second, the increase in the growth duration will also increase the diameter of the NRs, shown Fig. S3C in the

Supporting Information. This will reduce the porosity of the NR structure, which is defined as the percentage of open surface in the total top surface. This parameter determines the kinetics for the electrolyte transportation. Lower surface porosity results in restricted mass transportation with lower photocatalytic activity. By using the formula described in Fig. S8 in the Supporting Information, the surface porosities [40] of the M30, M60, M90 and M120 were calculated to be 47%, 42%, 33% and 27%, respectively. Third, if the radius of the nanorods is larger than the hole diffusion distance, the hole generated in the centre of the NR will have reduced probability of travel to the surface to react with the electrolyte. Under growth duration of 60 min, the radius of the ZnO NRs is about 330 nm, much larger than the hole diffusion distance for ZnO (~125nm) [3].

3.4.3 Enhanced photocatalytic activity with stacked mesh photoanodes

To further improve the photoconversion efficiency, we developed stacked, parallel multiple SS mesh photoanodes. In a stacked structure, it is expected that some light transmitted through the mesh will be trapped and reflected between electrodes. The light leakage through transmission can be effectively eliminated by using sufficient numbers of mesh photoanodes. The scheme of internal light scattering and absorption between SS meshes is shown in Fig. S9, Supporting Information.

As shown in Fig. S3A (Supporting Information), with increasing growth duration, the ZnO NRs became longer and the optical transmittance of the mesh gradually decreased. For the stacked photoanode, M60 samples were chosen since they have intermediate transmittance (22.5%) with good surface porosity (42%). The meshes were separated by 5mm. Fig. 9A shows the photocurrents generated from one to four parallel layers of M60 (named as 1L–4L) under 100 mW/cm^2 illumination between potentials of -0.5 and 1.0 $V_{Ag/AgCl}$.

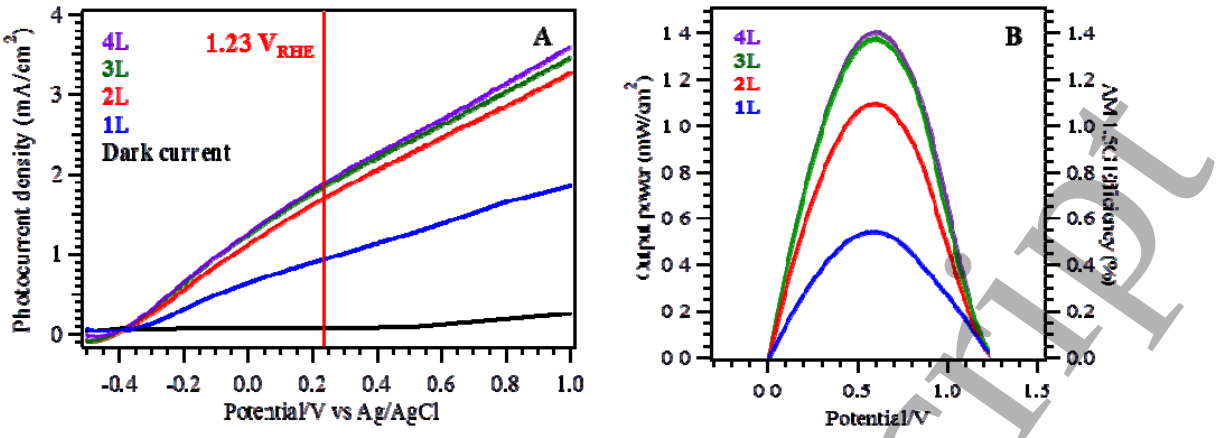

Fig. 9. (A) *I-V* curves of ZnO NRs with different number of layer of M60 together with dark current measured from 4L and (B) corresponding PEC output power and photo efficiency under AM1.5 G full solar spectrum irradiation.

In comparison to the 1L photoanode, the 2L and 3L photoanodes show significant enhancement in photocurrent densities. The photocurrent density appears to be saturated after 3L. The photocurrents measured at the potential of 1.23 V_{RHE} were 0.91, 1.70, 1.82 and 1.90 mA/cm^2 for the 1L, 2L , 3L and 4L samples respectively. The corresponding PEC output power and efficiency are presented in Fig. 9B, which shows the efficiency increase by 0.55% (1L), 1.10% (2L), 1.38% (3L) and 1.41% (4L), respectively. When compared with the 1L photoanode, the 4L photoanode demonstrates an improved PEC water splitting efficiency by a factor 2.6.

A UV-visible spectrophotometer was used to quantitatively assess the amount of light that passes through the multilayered photoanode. As shown in Fig. 10A, the optical transmission decreased when the number of layers of M60 increased. The optical transmission obtained from 1L, 2L, 3L and 4L photoanodes was 22.43%, 2.20%, 0.34% and 0.14%, respectively. This indicates a rapid exponential decrease of light leakage through transmission; when the number of stacked mesh is more than 4, such light leakage is almost completely eliminated. Fig. 10B shows that an inverse correlation was observed between the

optical transmission and photoconversion efficiency of multilayered stacked M60 photoanodes.

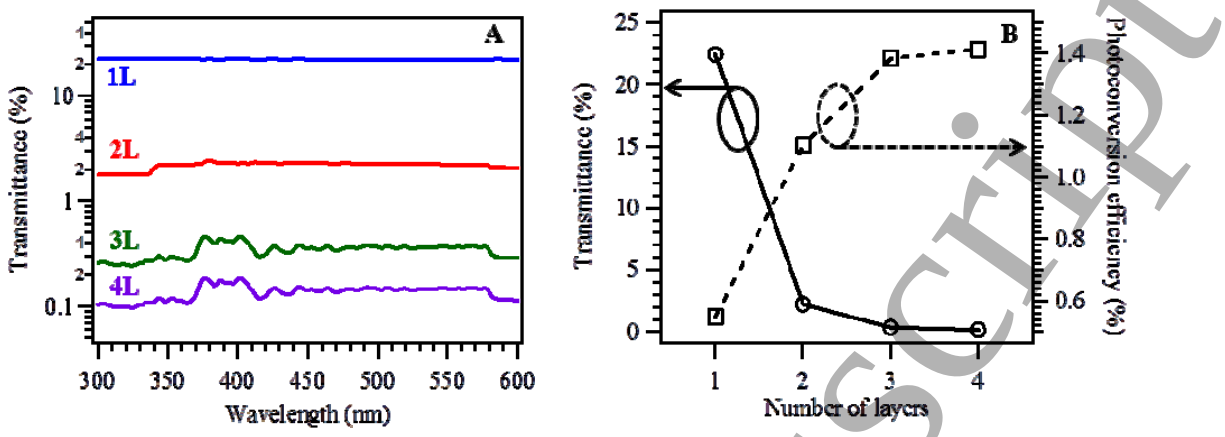

Fig. 10. (A) Optical transmission spectra of the samples for different number of stacked M60 mesh photoanodes and (B) plot of optical transmission and photoconversion efficiency with different number of stacked M60 photoanodes.

In comparison with the single mesh, the significant enhancement in photoconversion efficiency from multiple stacked photoanodes (4L) is attributed to the light trapping between the meshes due to internal reflections. Consequently, more light is being harvested and utilised by the material in the water splitting reaction. Such a stacked photoanode design represents a simple solution to improve light harvesting in a photoexcitation process. Meanwhile, the 3D stacked ZnO NR photoanode also offers a larger projected surface density of reaction centres, without restricting the ion transportation in the electrolyte. In comparison with the conventional flat substrate, such as the P15 photoanode, the stacked multilayer photoanode increases photoconversion by more than a factor of 6.1 (from 0.23% to 1.41%). For a plate substrate, light absorption is normally improved by increasing the ZnO film thickness. However, such an approach could restrict charge transportation within the film and increase charge recombination. With stacked mesh photoanodes, since each film thickness is reduced, this problem is effectively avoided.

4. Conclusions

We demonstrate for the first time an ultra-rapid direct heating synthesis of vertically aligned crystalline ZnO NR arrays on SS meshes. The final morphology of ZnO nanostructures is strongly affected by the growth condition. Increasing the applied heating power and growth duration increases the dimension and complexity of ZnO NR structures. The PEC water splitting measurements reveal that the SS mesh ZnO NR photoanode is over two times more efficient than the similar NR arrays on an SS plate. The transient *I-V* measurements show that the ZnO NRs grown using this DHS technique have slower charge recombination, while the EIS measurements suggest they have higher charge carrier density than those grown in a typical CBD process. The associated defects (oxygen vacancies) are possibly located on the surface of the ZnO NRs, which is responsible for the observed higher photoefficiency. We also demonstrate that the PEC water splitting efficiency could be further improved by 256% with stacked multiple parallel mesh photoanodes. With such a configuration, the transmitted light can be effectively trapped between the layers of electrodes with minimal light leakage.

5. References

[1] Ni M, Leung M K H, Leung D Y C, Sumathy K, 2007 *Renew. Sust. Energ. Rev.* **11** 401-425
[2] Xu S, Wang Z L, 2011 *Nano Res.* **4** 1013-1098
[3] Soudi A, Dhakal P, Gu Y, 2010 *Appl. Phys. Lett.* **96** 253115
[4] Kalanur S S, Hwang Y J, Chae S Y, Joo O S, 2013 *J. Mater. Chem. A* **1** 3479-3488
[5] Zhang Q F, Dandeneau C S, Zhou X Y, Cao G Z, 2009 *Adv. Mater.* **21** 4087-4108
[6] Chen H M, Chen C K, Chang Y C, Tsai C W, Liu R S, Hu S F, et al., 2010 *Angew. Chem. Int. Edit.* **49** 5966-5969
[7] Lee W C, Canciani G E, Alwhshe B O, Chen Q, 2016 *Int. J. Hydrogen Energy* **41** 123-131
[8] Dai H, Zhou Y, Liu Q, Li Z D, Bao C X, Yu T, et al., 2012 *Nanoscale* **4** 5454-5460
[9] Zhang J T, He M, Fu N Q, Li J Y, Yin X, 2014 *Nanoscale* **6** 4211-4216
[10] Wu C C, Wei L, Li Y T, Liu C, Jiao J, Chen Y X, et al., 2014 *Nanoscale Res. Lett.* **9** 112
[11] Khan S U M, Akikusa J, 1999 *J. Phys. Chem. B* **103** 7184-7189
[12] Fang Y, Lee W C, Canciani G E, Draper T C, Al-Bawi Z F, Bedi J S, et al., 2015 *Mat. Sci. Eng. B* **202** 39-45
[13] Lee Y J, Ruby D S, Peters D W, McKenzie B B, Hsu J W P, 2008 *Nano Lett.* **8** 1501-1505
[14] Fan X, Wang F Z, Chu Z Z, Chen L, Zhang C, Zou D C, 2007 *Appl. Phys. Lett.* **90** 073501
[15] Kuo M, Poxson D J, Kim Y S, Mont F W, Kim J K, Schubert E F, et al., 2008 *Opt. Lett.* **33** 2527-2529
[16] Wang J, Xia Y, Dong Y, Chen R, Xiang L, Komarneni S, 2016 *Appl. Catal. B* **192** 8-16
[17] Guo W X, Xu C, Wang X, Wang S H, Pan C F, Lin C J, et al., 2012 *J. Am. Chem. Soc.* **134** 4437-4441
[18] Liu Z Y, Misra M, 2010 *ACS Nano* **4** 2196-2200
[19] Dai H, Zhou Y, Chen L, Guo B L, Li A D, Liu J G, et al., 2013 *Nanoscale* **5** 5102-5108
[20] Lin C J, Chen S Y, Liou Y H, 2010 *Electrochem. Commun.* **12** 1513-1516
[21] Lee M R, Eckert R D, Forberich K, Dennler G, Brabec C J, Gaudiana R A, 2009 *Science* **324** 232-235
[22] Liu Z Y, Zhang Q Q, Zhao T Y, Zhai J, Jiang L, 2011 *J. Mater. Chem.* **21** 10354-10358
[23] Liu Z Y, Subramania V, Misra M, 2009 *J. Phys. Chem. C* **113** 14028-14033
[24] Wang M, Ren F, Zhou J, Cai G, Cai L, Hu Y, et al., 2015 *Sci. Rep.* **5** 12925
[25] Kajikawa Y, Noda S, Komiyama H, 2002 *Chem. Vap. Deposition* **8** 99-104
[26] Waterhouse G I N, Waterland M R, 2007 *Polyhedron* **26** 356-368
[27] Saito R, Miseki Y, Sayama K, 2012 *Chem. Commun.* **48** 3833-3835
[28] Parmar K P S, Kang H J, Bist A, Dua P, Jang J S, Lee J S, 2012 *ChemSusChem* **5** 1926-1934
[29] Moniz S J A, Zhu J, Tang J W, 2014 *Adv. Energy Mater.* **4** 1301590
[30] Wang M, Ren F, Cai G X, Liu Y C, Shen S H, Guo L J, 2014 *Nano Res.* **7** 353-364
[31] Mora-Sero I, Fabregat-Santiago F, Denier B, Bisquert J, Tena-Zaera R, Elias J, et al., 2006 *Appl. Phys. Lett.* **89** 203117
[32] Lin Y G, Hsu Y K, Chen Y C, Lee B W, Hwang J S, Chen L C, et al., 2014 *ChemSusChem* **7** 2748-2754
[33] Rusu D I, Rusu G G, Luca D, 2011 *Acta Phys. Pol. A* **119** 850-856
[34] Wang G M, Wang H Y, Ling Y C, Tang Y C, Yang X Y, Fitzmorris R C, et al., 2011 *Nano Lett.* **11** 3026-3033

[35] Tafalla D, Salvador P, Benito R M, 1990 *J. Electrochem. Soc.* **137** 1810-1815
[36] Li Z D, Yao C H, Yu Y H, Cai Z Y, Wang X D, 2014 *Adv. Mater.* **26** 2262-2267
[37] Li J T, Cushing S K, Zheng P, Meng F K, Chu D, Wu N Q, 2013 *Nat. Commun.* **4** 2651
[38] Martinson A B F, McGarrah J E, Parpia M O K, Hupp J T, 2006 *Phys. Chem. Chem. Phys.* **8** 4655-4659
[39] Zhang X Y, Qin J Q, Xue Y N, Yu P F, Zhang B, Wang L M, et al., 2014 *Sci. Rep.* **4**
[40] Lee W C, Fang Y X, Kler R, Canciani G E, Draper T C, Al-Abdullah Z T Y, et al., 2015 *Mater. Chem. Phys.* **149** 12-16